Biosensors and Bioelectronics 135 (2019) 145–152

Contents lists available at ScienceDirect

Biosensors and Bioelectronics

journal homepage: www.elsevier.com/locate/bios

Oxygen vacancy enhanced photoelectrochemical performance of Bi_2MoO_6/B, N co-doped graphene for fabricating lincomycin aptasensor

Lan Ge[a], Qian Liu[a,**], Ding Jiang[a], Lijun Ding[a], Zuorui Wen[a], Yingshu Guo[b,***], Caifeng Ding[c], Kun Wang[a,c,*]

[a] Key Laboratory of Modern Agriculture Equipment and Technology, School of Chemistry and Chemical Engineering, Jiangsu University, Zhenjiang, 212013, PR China
[b] Collaborative Innovation Center of Tumor Marker Detection Technology, Equipment and Diagnosis-Therapy Integration in Universities of Shandong, Shandong Province Key Laboratory of Detection Technology for Tumor Makers, School of Chemistry and Chemical Engineering, Linyi University, Linyi, 276005, PR China
[c] Qingdao Univ Sci & Technol, Key Laboratory of Optic-electric Sensing and Analytical Chemistry for Life Science, OE, Coll Chem & Mol Engn, Qingdao, 266042, PR China

ARTICLE INFO

Keywords:
Oxygen vacancy
Boron and nitrogen co-doped graphene
Bi_2MoO_6 nanoparticle
Photoelectrochemical aptasensor
Lincomycin

ABSTRACT

Oxygen defect-engineered is an important strategy to improve the photoelectric activity of materials. Herein, a facile one-pot solvothermal method was utilized to synthesize visible light-responsive photoactive Bi_2MoO_6 nanoparticles anchored boron and nitrogen co-doped graphene (BNG) nanosheets nanocomposites with oxygen vacancy. The incorporation of BNG nanosheets increased the oxygen vacancies amounts on Bi_2MoO_6 remarkably, and the presences of oxygen vacancies can be beneficial to broaden the absorption range. The absorption edge of Bi_2MoO_6/BNG was widened from 500 nm to 550 nm compared to Bi_2MoO_6, and the charge transfer was accelerated to improve the photoactive of Bi_2MoO_6/BNG. Under visible light illumination, the photoelectrochemical (PEC) response of the as-prepared Bi_2MoO_6/BNG was 11.6-fold, 6.7-fold, 3.1-fold and 2.4-fold higher than that of pristine Bi_2MoO_6, Bi_2MoO_6/graphene, Bi_2MoO_6/nitrogen doped graphene and Bi_2MoO_6/boron doped graphene. Using Bi_2MoO_6/BNG nanocomposites with the superior PEC performance as photoactive materials in combination with specifically recognized lincomycin (LIN) aptamer, a highly efficient PEC aptasensor was successfully constructed for sensitive analysis of LIN. Under optimal conditions, the proposed PEC aptasensor exhibited excellent analytical performance for LIN with a wide linear response of 1×10^{-11} to 1×10^{-6} mol L^{-1} along with a low detection limit of 3.7×10^{-12} mol L^{-1} (defined as $S/N = 3$). The as-prepared Bi_2MoO_6/BNG nanocomposites exhibit excellent visible light response and PEC performance, indicating its potential applications in PEC biosensor.

1. Introduction

The photoelectrochemical (PEC) sensor, as a late-model sensing technique based on efficient photo-to-electric conversion, has attracted huge concern due to its excellent analytical property (Zhao et al. 2014, 2015). From the evolution of traditional electrochemical detection methods, the PEC sensors are widely applied in food safety, environmental monitoring and bioanalysis due to high sensitivity, low cost and simple instruments (Yue et al., 2013; Li et al., 2016). Currently, the further development of PEC biosensor mainly focus on the following aspects: (1) new strategy is adopted to fabricate PEC sensing systems to improve analytical performance and eliminate interference, such as a ratiometric PEC sensor is built to remove interference and provide a better accuracy (Hao et al., 2017b; Zhang et al., 2017); (2) designing photoactive materials that can respond to visible or near-infrared light to achieve signal amplification strategies (Qiu et al., 2018). Great efforts have been devoted to design photoactive metal semiconductors with high photoelectric separation efficiency and biocompatibility in the field of PEC biosensor (Zhuang et al., 2015).

Recently, a large number of studies have demonstrated that intrinsic defects and extrinsic impurities in metal oxide semiconductors have a significant effect on some important physicochemical properties (Wang et al., 2015). Oxygen vacancy is one of the common defects, and its introduction can be conductive to broaden the range of absorption,

* Corresponding author. Key Laboratory of Modern Agriculture Equipment and Technology, School of Chemistry and Chemical Engineering, Jiangsu University, Zhenjiang, 212013, PR China.
** Corresponding author.
*** Corresponding author.
E-mail addresses: liuqian@ujs.edu.cn (Q. Liu), yingshug@126.com (Y. Guo), wangkun@ujs.edu.cn (K. Wang).

https://doi.org/10.1016/j.bios.2019.04.022
Received 19 March 2019; Received in revised form 9 April 2019; Accepted 11 April 2019
Available online 16 April 2019
0956-5663/

narrow the band gap, increase the active sites and improve the efficiency of charge separation (Wang et al., 2018; Wu et al., 2018). In our previous work, Eu_2O_3/g-C_3N_4 nanocomposite with oxygen vacancy was prepared for the fabrication of sensitive electrochemiluminescence (ECL) sensor (Du et al., 2018). Tang et al. also prepared defect-engineered TiO_{2-x} as photoactive materials for the construction of PEC biosensors (Shu et al., 2018). The introduction of oxygen vacancy can be achieved by a method of reduction and calcination. It is worth noting that these methods are hard to achieve oxygen vacancies on semiconductors, which requires complex, rigorous or high-risk conditions, such as high temperature and hydrogen atmosphere (Xu et al., 2019). Thus, we consider that it is meaningful to use a gentle and facile method to synthetize high-performance photoactive materials with oxygen vacancy for the fabrication of PEC biosensor.

Aurivillius-phase bismuth molybdate (Bi_2MoO_6) has been considered as the forefront of efficient visible-light driven photoactive materials owing to eco-friendly and relatively suitable bandgap (2.5–2.8 eV) (Tian et al., 2015; Wang et al., 2017). However, the visible-light-responsive photoactive of Bi_2MoO_6 possess poorly due to its slow carrier transferring, rapid recombination of electron-hole, and poor surface chemical states (Meng et al., 2018). It has been reported in the literature that there is a synergistic effect between oxygen vacancies and precious metal deposition, which can be used as a feasible method to improve the photoactivity of Bi_2MoO_6 (Zheng et al., 2017). Graphene-based nanomaterials can function as ideal candidates for advanced function biosensor due to its large surface area, excellent electrical conductivity and biocompatibility (Hao et al., 2018; Ma et al., 2014). To improve the property of graphene, it is an effective method to replace some carbon atoms of graphene with heteroatoms, for instance N, B, P and S, which can effectively change the properties of electron donor and resulting in an increase its activity (Liu et al., 2011; Yang et al., 2012). In particular, since the electronegativity of C (2.55) is between B (2.05) and N (3.04), a unique electronic structure can be generated, creating a synergistic effect with heteroatoms (Zheng et al., 2013). With these respects taken into consideration, it is logical to explore the coupling of Bi_2MoO_6 with B and N co-doped graphene (BNG) and introducing oxygen vacancies, and as a photoactive material with excellent performance.

Lincomycin (LIN) derived from streptomycin lincolnensis is a narrow spectrum antibiotic that inhibits Gram-positives bacteria and has been widely applied in human and veterinary (Li et al., 2017). Some studies have indicated that the residue of LIN in animal-derived foodstuffs may produce some adverse effect, such as allergic reactions and bacterial resistance (Zhou et al., 2014). Some research has indicated that the residue of LIN in animal-derived foodstuffs may produce some adverse effect, such as allergic reactions and bacterial resistance (Zhou et al., 2014). The maximum residue limits (MRLs) of LIN stipulated by the U.S. Food and Drug administration are 3.4×10^{-7} mol L^{-1} for milk and 2.3×10^{-7} mol L^{-1} for the edible tissues of chicken and swine (Chiu et al., 2009). Various classical methods have been explored for analysis of LIN, such as HPLC (Stypulkowska et al., 2015), Chemiliminescence (Yang et al., 2010), Fluorescence (Zhou et al., 2014) and Electrochemical (Chiu et al., 2009). These methods can be utilied for the detection of LIN owing to their high accuracy, however they all have some disadvantages, for example complicated operation, time-consuming, large-scale instruments, low sensitivity. Thus, it is necessary to develop an uncomplicated, rapid and cost-effective detection ways for the sensitive determination of LIN. Here, Bi_2MoO_6 nanoparticles are loaded on BNG nanosheets to form excellent photoactive nanocomposites by facile one-pot solvothermal route for the first time, ethylene glycol (EG) as a reducing agent causes the appearance of oxygen vacancy in Bi_2MoO_6 (Liu et al., 2017). The introduction of oxygen vacancy and BNG could be capable to accelerate charge transfer efficiency and curb the recombination of electron-hole pairs, resulting in Bi_2MoO_6/BNG possessing an excellent PEC performance compared to BNG, Bi_2MoO_6. Based on wonderful PEC performance of Bi_2MoO_6/BNG nanocomposites, a sensitive PEC aptsensor for LIN detection was fabricated, which was applied to real samples to ensure practicality, demonstrating Bi_2MoO_6/BNG can be utilized as potential visible light-driven photoactive nanomaterial for PEC sensor.

2. Experimental section

2.1. Reagents and chemicals

$Bi(NO_3)_3{\cdot}5H_2O$, $Na_2MoO_4{\cdot}2H_2O$, $(NH_4)_2B_{10}O_{16}{\cdot}8H_2O$, glycine, H_3BO_3, EG and N,N-dimethylformamide (DMF) was acquired from Sinopharm Chemical Reagent Co., Ltd. Graphene oxide powder was purchased from Nanjing Xianfeng Nano Materials Technology Co., Ltd. LIN aptamer: 5′-CGCG TGAT GTGG TCGA TGCG ATAC GGTG AGTC GCGC CACG GCTA CACA CGTC TCAG CGA- 3′ was acquired from Sangon Biotech Co., Ltd. (shanghai, China). Lincomycin hydrochloride and other antibiotics were purchased from Aladin Reagent Co., Ltd. (Shanghai, China). All PEC experiments were carried out at phosphate buffered saline (PBS, 0.1 mol L^{-1}, pH 7.4) as the supporting electrolyte. All of the other chemical reagents were applied as received with the analytical grade. Ultrapure water (> 18.2 MΩ cm, Mili-Q, Millipore) was employed whole the study.

2.2. Preparation of Bi_2MoO_6/BNG

Bi_2MoO_6/BNG was prepared through a one-pot solvothermal route. First of all, 0.2425 g $Bi(NO_3)_3{\cdot}5H_2O$ and 0.065 g $Na_2MoO_4{\cdot}2H_2O$ were respectively dispersed in 5 mL EG and vigorously stirred at 60 °C. Then, the $Na_2MoO_4{\cdot}2H_2O$ solution was dropwised into the $Bi(NO_3)_3{\cdot}5H_2O$ solution with stirring and named solution A. After that, a certain amount of GO and 100 mg $(NH_4)_2B_{10}O_{16}{\cdot}8H_2O$ were scattered in 10 mL EG with ultrasonic to obtain well-distributed solution and named solution B. Afterwards, the solution B was slowly dropwised into the solution A and magnetically stirred for 1 h. At last, the suspension was transferred into Teflon-lined stainless steel and maintained 160 °C for 24 h. The samples were obtained by centrifugation and dried at 60 °C under oven. The Bi_2MoO_6/BNG nanocomposites with different rations of GO to Bi_2MoO_6 (4, 6, 8, 10 and 12 wt%) were synthesized using the same procedure. For comparison, the Bi_2MoO_6 were prepared without the addition of GO and $(NH_4)_2B_{10}O_{16}{\cdot}8H_2O$ under the same experimental conditions, and BNG were obtained without appending $Bi(NO_3)_3{\cdot}5H_2O$ and $Na_2MoO_4{\cdot}2H_2O$. In addition, the Bi_2MoO_6/graphene (Bi_2MoO_6/G), were prepared without the addition of $(NH_4)_2B_{10}O_{16}{\cdot}8H_2O$, Bi_2MoO_6/nitrogen doped graphene (Bi_2MoO_6/NG), Bi_2MoO_6/boron doped graphene (Bi_2MoO_6/BG) were prepared by replacing $(NH_4)_2B_{10}O_{16}{\cdot}8H_2O$ with glycine and H_3BO_3, respectively.

2.3. Fabrication of the modified electrodes

Primarily, the indium tin oxide (ITO) electrodes were placed in boiling 1 mol L^{-1} of NaOH and then ultrasonically cleaned in deionized water and alcohol. 5 mg of Bi_2MoO_6/BNG was scattered in 1.0 mL of DMF under ultrasonic agitation to obtained 5 mg mL^{-1} Bi_2MoO_6/BNG suspension. Then, 40 μL of the Bi_2MoO_6/BNG suspension were dropped on ITO electrode surface with exposed geometric area of 0.5 cm^2 and then dried under the infrared lamp to get Bi_2MoO_6/BNG modified ITO electrode (Bi_2MoO_6/BNG/ITO). For comparison, Bi_2MoO_6/ITO, BNG/ITO, Bi_2MoO_6/G/TO, Bi_2MoO_6/NG/ITO and Bi_2MoO_6/BG/ITO were got in the similar procedure, respectively.

2.4. Fabrication of the PEC aptasensor

The LIN PEC aptasensor fabrication process was shown as follows, 20 μL of 2×10^{-6} mol L^{-1} LIN aptamer solution were immobilized on the Bi_2MoO_6/BNG/ITO, dried at air temperature and rinsed with PBS to remove excess non-adsorbed aptamers. Then, the aptamer Bi_2MoO_6/

BNG/ITO electrode was incubated in the different concentrations of LIN solution at air temperature and followed by washed thoroughly 0.1 mol L^{-1} PBS and subjected to PEC measurements.

2.5. Photoelectrochemical measurement

The PEC measurements were recorded with CHI660B electrochemical workstation (Chenhua Instrument Co. Ltd., Shanghai China). The PEC test with a conventional three-electrode system were employed in 0.1 mol L^{-1} PBS at 0 V and a 250 W Xe lamp (CHF-XM35-500W, Beijing Chang tuo) was used as the visible-light source with a 400 nm UV-cut filter. Electrochemical impedance spectroscopy (EIS) was carried out in the 0.1 mol L^{-1} KCl solution containing 5 mmol L^{-1} $[Fe(CN)_6]^{3-/4-}$ with a frequency range from 0.01 Hz to 10 kHz at a constant potential of 0.23 V. Cyclic voltammograms (CVs) experiments were recorded in 5 mmol L^{-1} $[Fe(CN)_6]^{3-/4-}$ with the potential rang from −0.4–0.8 V at scan rate of 100 mV/s.

3. Results and discussion

3.1. Characterization of the samples

The morphology of Bi_2MoO_6 and Bi_2MoO_6/BNG were employed by Transmission electron microscope (TEM). As displayed in Fig. 1A, the particle size of Bi_2MoO_6 nanoparticles is 10–20 nm, and the self-agglomerated is serious. By introducing of BNG nanosheets, Bi_2MoO_6 nanoparticles were uniformly dispersed on the surface of BNG nanosheets (Fig. 1B). Furthermore, the elemental mapping images (EMIs) are displayed in Fig. S1 indicated that Bi, Mo, O, B, C, and N elements are uniformly spread throughout the Bi_2MoO_6/BNG nanocomposites.

X-ray diffraction (XRD) patterns were applied to determine the crystalline property of the as-fabricated BNG, Bi_2MoO_6 and Bi_2MoO_6/BNG as shown in Fig. 1C. The Bi_2MoO_6 showed the diffraction peaks at 2θ = 28.36°, 32.64°, 36.12°, 46.86°, 55.62° and 58.52°, which might be assigned to the (131), (002), (151), (202), (133) and (262), respectively. All the diffraction peaks were unambiguously ascribed to the orthorhombic Bi_2MoO_6 nanoparticles (JCPDS No. 21–0102) and no other peaks were observed, proving the acquired samples of high purity (Wang et al., 2017). The XRD pattern of Bi_2MoO_6/BNG was practical unanimity compared with the Bi_2MoO_6, and no obvious peak of BNG is observed suggesting the BNG nanosheets did not overlap on each other and Bi_2MoO_6 nanoparticles were homogeneously dispersed the surface of BNG nanosheets (Zhang et al., 2014).

Raman spectroscopy were utilized in the properties of structure and defects of graphene-based nanocomposites (Hao et al., 2017a). As shown in Fig. 1D, the strong bands in the range of 200–1000 cm^{-1} are corresponded to the vibrational modes of orthorhombic Bi_2MoO_6 (curve b). The bands between 700-850 cm^{-1} are ascribed to the symmetric stretch of MoO_6 octahedra (Sun et al., 2017), and the Raman bands at 230-460 cm^{-1} attributing to the bending modes of the MoO_6 octahedra and BiO_3 tetrahedra (Zheng et al., 2017), respectively. The Raman spectrum of BNG and Bi_2MoO_6/BNG possessed two remarkable peaks at 1349 and 1596 cm^{-1}, attributing to the D and G bands, respectively. The D band is attributed to the structural defects, while the G band can be assigned to the graphitic hexagon-pinch mode (Ge et al., 2018). Evidently, the intensity ratio of I_D/I_G (1.18) of Bi_2MoO_6/BNG was higher than BNG (1.03), which suggesting that there were many defects in the Bi_2MoO_6/BNG nanocomposite. The defects of Bi_2MoO_6/BNG might be beneficial to enhance the PEC properties of the nanocomposites (Zhang et al., 2012).

To investigate the oxygen vacancies production and element constituent of Bi_2MoO_6/BNG nanocomposites, X-ray photoelectron spectrometry (XPS) analysis has been applied. As illustrated in Fig. 2A, the survey spectrum of Bi_2MoO_6/BNG demonstrated that this composite was comprised of six elements: Bi, Mo, O, C, N and B, respectively. The deconvoluted N 1s XPS spectrum (Fig. 2B) showed three peaks at 396.2 eV, 397.8 eV and 399.0 eV, which were assigned to the N—B, N—C and graphite N (Zheng et al., 2013). Furthermore, the high resolution of B 1s (Fig. 2C) showed that two peaks at 189.2 eV and 190.2 eV were ascribed to B—C and B—N, respectively (Choi et al.,

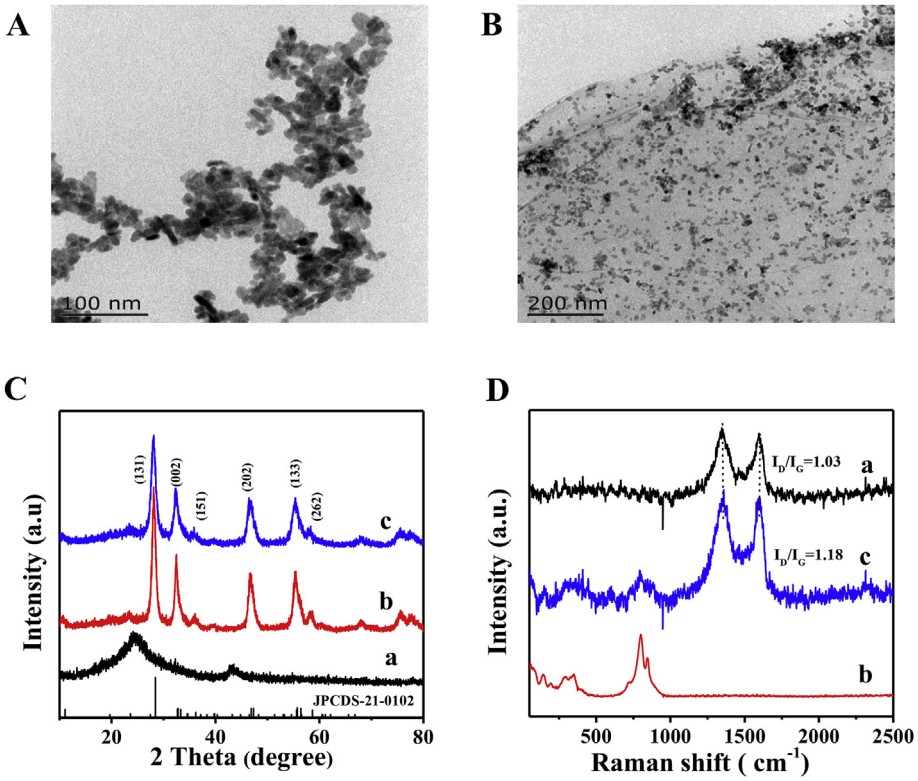

Fig. 1. TEM images of (A) Bi_2MoO_6 and (B) Bi_2MoO_6/BNG. (C) XRD patterns and (D) Raman spectra of BNG (a), Bi_2MoO_6 (b) and Bi_2MoO_6/BNG (c).

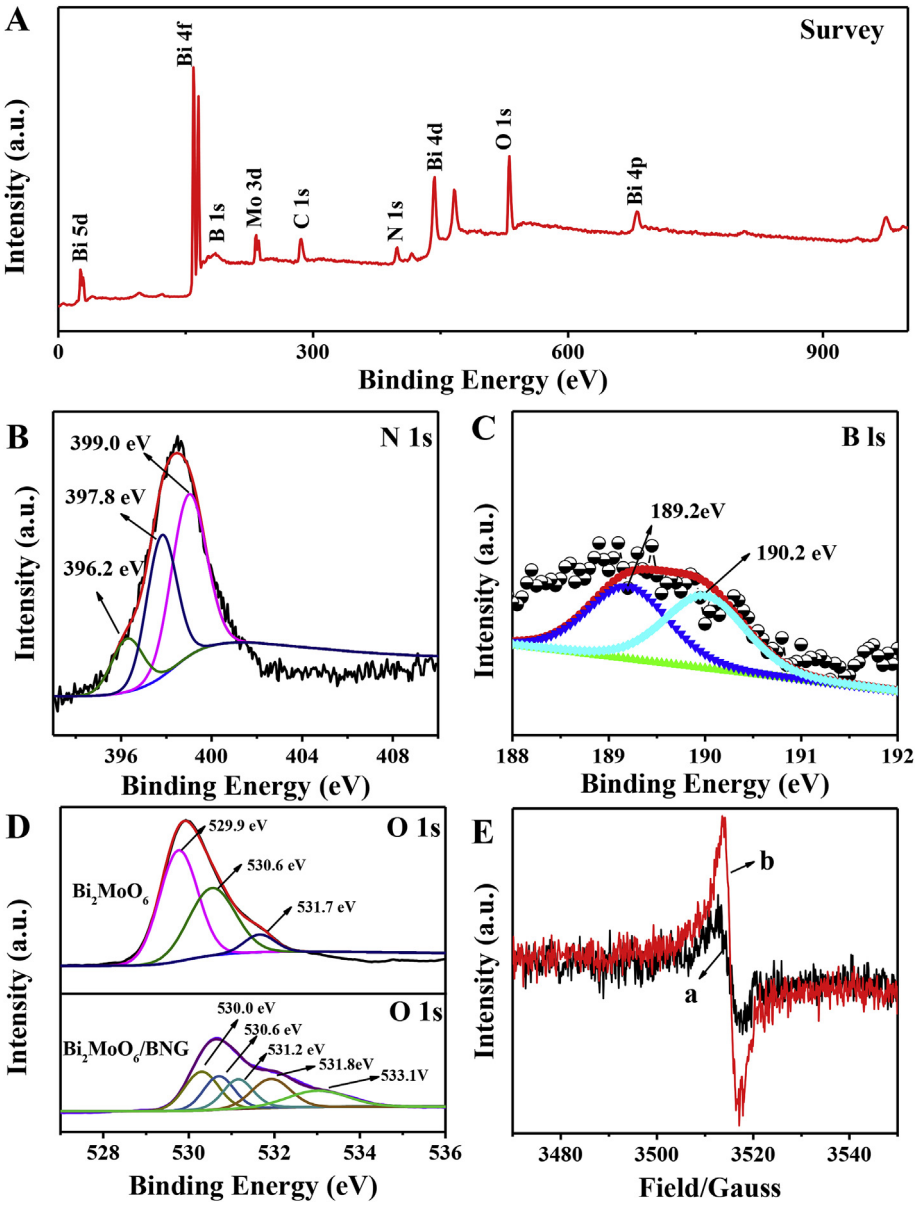

Fig. 2. (A) XPS survey of Bi_2MoO_6/BNG, (B) N 1s, (C) B 1s, (D) O 1s spectra and (E) EPR spectra of Bi_2MoO_6 (a) and Bi_2MoO_6/BNG (b).

2012). Two peaks at 158.9 eV and 164.3 eV can be indexed to Bi $4f_{7/2}$ and Bi $4f_{5/2}$ (Zhu et al., 2017) (Fig. S2A). The Mo 3d observed at 232.1 eV and 235.3 eV were ascribed to Mo $3d_{5/2}$ and Mo $3d_{3/2}$ (Zheng et al., 2017) (Fig. S2B). In the spectrum of C 1s (Fig.S2C) displayed three peaks at 283.9, 285.6 and 288.4 eV, which were assigned to C—B, C—C and C—N bonding in Bi_2MoO_6/BNG nanocomposites (Qian et al., 2015). The O 1s XPS spectra in Bi_2MoO_6 and Bi_2MoO_6/BNG are displayed in Fig. 2D. For Bi_2MoO_6, there are two peaks at 529.9 eV and 530.6 eV, respectively, which belong to Bi—O and Mo—O. In addition, the peak appearing at 531.7 eV can be ascribed to the presence of oxygen vacancies in the host lattice (Zheng et al., 2017). compared with pristine Bi_2MoO_6, the O 1s XPS spectra in Bi_2MoO_6/BNG has four peaks at 530.0, 530.6, 531.2 and 533.1 eV, respectively, which can be attributed to Bi—O, Mo—O, C—O and C═O (Meng and Zhang, 2017). In particular, a peak appearing at 531.8 eV belongs to the oxygen vacancy, and the intensity is stronger, indicating that the incorporation of BNG can enhance the oxygen vacancies amounts of Bi_2MoO_6.

Then, Electron paramagnetic resonance (EPR) was utilized to further verify the existence of oxygen vacancies. As clearly shown in Fig. 2E, obvious EPR signals at g = 2.002 corresponding to oxygen vacancies are observed for Bi_2MoO_6 and Bi_2MoO_6/BNG (Wu et al., 2018). Furthermore, the intensity of oxygen vacancies EPR signal in Bi_2MoO_6/BNG is significantly higher than that in Bi_2MoO_6, indicating the introduction of BNG can increase the amount of oxygen vacancies. These above results indicated that the as-fabricated oxygen vacancies engineered Bi_2MoO_6/BNG nanocomposite has been successfully prepared.

3.2. Photoelectrochemical measurements

The UV-visible absorption spectroscopy of BNG, Bi_2MoO_6 and Bi_2MoO_6/BNG were displayed in Fig. 3A. As can be seen, the BNG has light absorption over the entire wavelength range, this is a typical characteristic of graphene. The absorption band edge of Bi_2MoO_6 are around 500 nm which basically the same as the data reported in the literature (Zou et al., 2014). The Bi_2MoO_6/BNG exhibits broader absorption in the visible region comparing with Bi_2MoO_6. As can be seen in Fig. 3B, the bandgap of Bi_2MoO_6/BNG was reduced to be 2.42 eV, which is smaller than that of 2.62 eV of pristine Bi_2MoO_6 (Tian et al., 2015). This phenomenon probably be ascribed to the existence of BNG

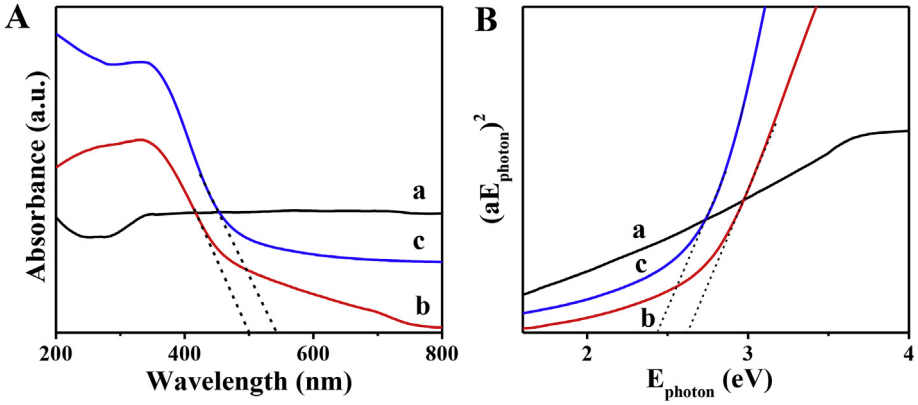

Fig. 3. (A) UV-vis diffuse reflectance spectra and (B) Plots of $(Ah\upsilon)^2$ versus the energy ($h\upsilon$) for the bandgap energy of BNG (a), Bi_2MoO_6 (b) and Bi_2MoO_6/BNG (c).

with no bandgap (curve a) (Liu et al., 2015) and oxygen vacancies can broaden the range of absorption and reduce band gap (Shu et al., 2018). The absorption enhancement and bandgap narrowing were advantage to enhance the photoelectrochemical performance of Bi_2MoO_6/BNG nanocomposite.

The PEC signal of different modified electrodes was explored in Fig. 4A. The PEC response of BNG (curve a) could be ignored and a weak PEC signal of the pristine Bi_2MoO_6 (0.65 ± 0.013 μA) was discovered (curve b). When Bi_2MoO_6 and BNG form nanocomposites, the photocurrent response of Bi_2MoO_6/BNG/ITO are significantly enhanced to 7.57 ± 0.14 μA, which was about 11.6-fold strengthened than that of Bi_2MoO_6/ITO. This reason might be attributed that the BNG nanosheets and oxygen vacancies could promote efficient charge separation and restrain the rapid electron-hole recombination, result in the enhanced PEC performance of Bi_2MoO_6/BNG. Furthermore, to explore the superiority boron and nitrogen co-doped graphene in the PEC response, the PEC value of Bi_2MoO_6/G/ITO, Bi_2MoO_6/NG/ITO and Bi_2MoO_6/BG/ITO were presented. The photocurrent intensity of Bi_2MoO_6/BNG was 6.7-fold, 3.1-fold and 2.4-fold enhancement than Bi_2MoO_6/G/ITO, Bi_2MoO_6/NG/ITO and Bi_2MoO_6/BG/ITO, which might be ascribed to the introduction of boron and nitrogen elements was in favor to inhibit recombination of electron-holes and accelerate charge transfer (Chen et al., 2018). To investigate the electron transfer procedure of the modified electrodes, EIS measurements of the BNG/ITO, Bi_2MoO_6/ITO, Bi_2MoO_6/G/ITO, Bi_2MoO_6/NG/ITO, Bi_2MoO_6/BG/ITO and Bi_2MoO_6/BNG/ITO were provided. As displayed in Fig. 4B, the electron-transfer resistance (R_{et}) value of BNG/ITO, Bi_2MoO_6/ITO, Bi_2MoO_6/G/ITO, Bi_2MoO_6/NG/ITO, Bi_2MoO_6/BG/ITO and Bi_2MoO_6/BNG/ITO was about 18, 108, 93, 84, 64 and 48 Ω, respectively. It can be found that the R_{et} of BNG is the smallest, and Bi_2MoO_6/BNG is second only to the R_{et} of BNG relative to other nanocomposites, indicating the introduction of boron and nitrogen elements, the presence of graphene sheet and oxygen vacancies can be beneficial to promote the charge transfer efficiency and inhibit the electron-holes recombination (Kecsenovity et al., 2017; Yu et al., 2016).

3.3. Fabrication of the PEC aptasensor

Fig. 5A displayed a schematic of PEC aptasensor for specifically detecting LIN. Under visible light illumination, the photoinduced electrons are transferred to the conduction band (CB) of Bi_2MoO_6 nanoparticles while holes migrate to the valence band (VB). The excellent electroconductivity of BNG nanosheets and oxygen vacancies can accelerate the electrons transfer to the ITO electrodes, and the photo-induced electrons and holes recombination are inhibited, leading to a powerful PEC response. Then in the introduction of aptamers molecules, the steric hindrance of the electrode interface and block the electron transfer were enhanced due to the appearance of aptamer (Yan et al., 2015), resulting in the PEC signal drastically diminish. When LIN molecules are appeared, the photo-induced holes can oxidize LIN that form complex with the aptamers (Augugliaro et al., 2005). Thus, the holes are reduced while electrons are greatly increased and driven to the ITO electrodes, leading to an increase in photocurrent in the presence of LIN molecules. These above PEC response results were also shown in Fig. 5B, indicating the fabricated PEC aptasensor could be applied for the analysis of LIN.

To further evaluate the successful step by step assembly process of PEC aptasensor, EIS and CVs measurements was utilized. Fig. 5C displayed the R_{et} from different modified electrodes associated with each fabrication process of the aptasensor. With the LIN aptamer assemble on Bi_2MoO_6/BNG modified electrode, the increase of value R_{et} from 63.6 to 103.9 Ω, which assigned to that aptamers were successfully bonded on the Bi_2MoO_6/BNG surface through the π−π stacking. The aptasensor could capture the LIN molecules when LIN molecules

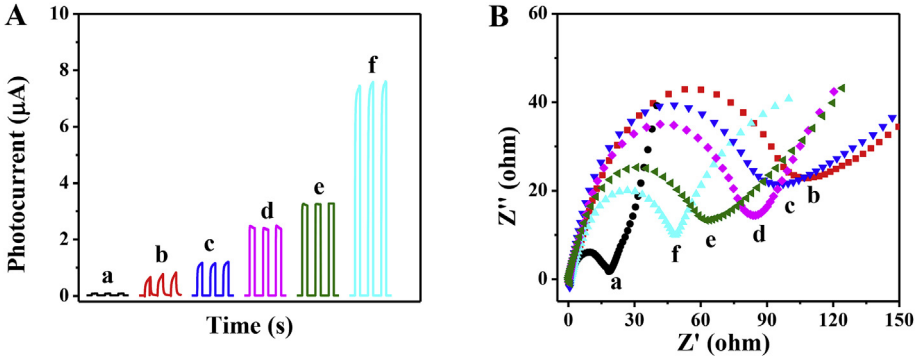

Fig. 4. (A) PEC signal and (B) Nyquist plots of BNG/ITO (a), Bi_2MoO_6/ITO (b), Bi_2MoO_6/G/ITO (c), Bi_2MoO_6/NG/ITO (d), Bi_2MoO_6/BG/ITO (e) and Bi_2MoO_6/BNG/ITO (f).

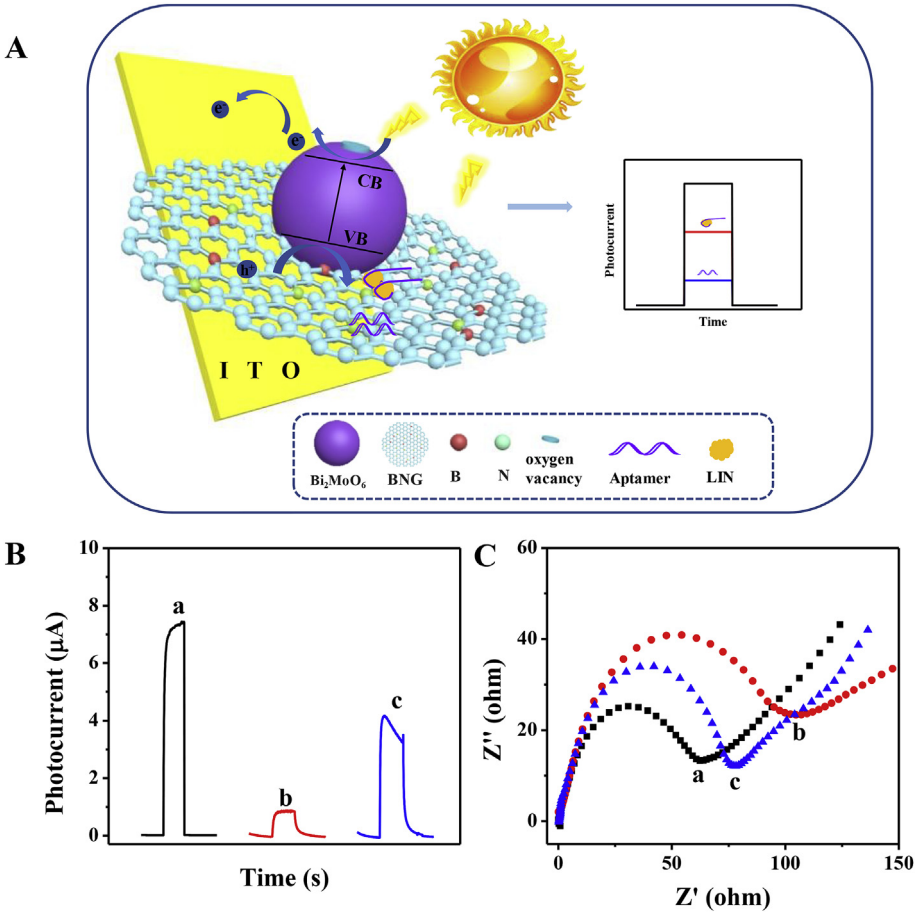

Fig. 5. (A) Schematic diagram of the established PEC aptasensor for determination LIN using Bi_2MoO_6/BNG nanocomposite. (B) Photocurrent responses and (C) Nyquist plots of Bi_2MoO_6/BNG/ITO (a), aptamer-Bi_2MoO_6/BNG/ITO (b) and LIN/aptamer- Bi_2MoO_6/BNG/ITO (c).

appear, the R_{et} of LIN/aptamer- Bi_2MoO_6/BNG/ITO reduced to 77.2 Ω. The reason might be ascribed to aptamer and LIN molecules formed a LIN-aptamer complex (Okoth et al., 2017).

In addition, Fig. S4 presented the CVs of different modified electrodes in fabrication process of PEC aptasensor. When LIN aptamers was introduced, there is an obvious peak at 0.35 V, and the peak current was significantly lower than that of Bi_2MoO_6/BNG/ITO. In the presence of LIN molecules, the peak current was increased. This phenomenon is consistent with the conclusions obtained in the EIS analysis. Therefore, all these results demonstrated that the established PEC aptasensor can be applied to the quantitative detection of LIN.

3.4. Optimization of experimental conditions

In order to fabricate a high efficiency and sensitivity PEC aptasensor, some important factor affecting PEC performance need to be optimized. Different content of GO in Bi_2MoO_6/BNG nanocomposites has great influence on photocurrent response and need to be optimized. Fig. S3A displayed the PEC response of Bi_2MoO_6/BNG with different GO contents. As shown, the PEC signals of Bi_2MoO_6/BNG with the percent of GO increased from 0 to 10% enhanced gradually. This phenomenon may be due to the reason that BNG can accelerate the charge separation efficiency. Thus, the PEC aptasensor selected $Bi_2MoO_6/BNG_{10\%}$ as the optimal photo response nanocomposite.

In addition, the aptamer concentration had an obvious effect the analysis property of the established aptasensor. Fig. S3B presented that when with the concentration of aptamer increasing from 1×10^{-7} to 2×10^{-6} mol L^{-1}, the photocurrent intensity gradually decreased and arrived a bottleneck when up to 2×10^{-6} mol L^{-1}. Thus, 2×10^{-6} mol L^{-1} was chosen to be the optimized aptamer concentration.

3.5. Sensitive and selective PEC aptasensor of LIN

Based on this optimal experimental conditions and excellent photoactive material of Bi_2MoO_6/BNG, a sensitive PEC aptasensor was successfully established for quantitative analysis of LIN. Fig. 6A records the PEC behavior of the aptasensor toward different concentration of LIN. It can be clearly seen that the PEC response gradually increased with the LIN concentration increasing. As illustrated in Fig. 6B, a good calibration curve was obtained between the logarithm of LIN concentration and PEC signal of the aptasensor in range of 1×10^{-11} mol L^{-1} to 1×10^{-6} mol L^{-1} ($R^2 = 0.992$). Furthermore, The corresponding linear equation is $I = 7.655 + 0.648\lg[C_{LIN}$ (mol·L^{-1})], the detection limit of the PEC aptasensor was estimated to be 3.7×10^{-12} mol L^{-1} (defined as $S/N = 3$). Therefore, compared with these previous reported methods for LIN analysis, the as-fabricated PEC aptasensor exhibited the wide liner response and relatively low detection limit (Table S1).

The specificity of the proposed aptasensor was explored by recording the PEC intensity of other antibiotics including tetracycline (TET), streptomycin (STR), chloramphenicol (CAP), ampicillin (AMP) and food additives (citric acid). It could be obviously observed that 1×10^{-7} mol L^{-1} of other interfering antibiotics have no significant PEC signal changes on the aptasensor compared with 1×10^{-8} mol L^{-1} of LIN (Fig. 6C), indicating the excellent selectivity of the proposed aptasensor.

Fig. 6D showed that the photocurrent intensity of the constructed

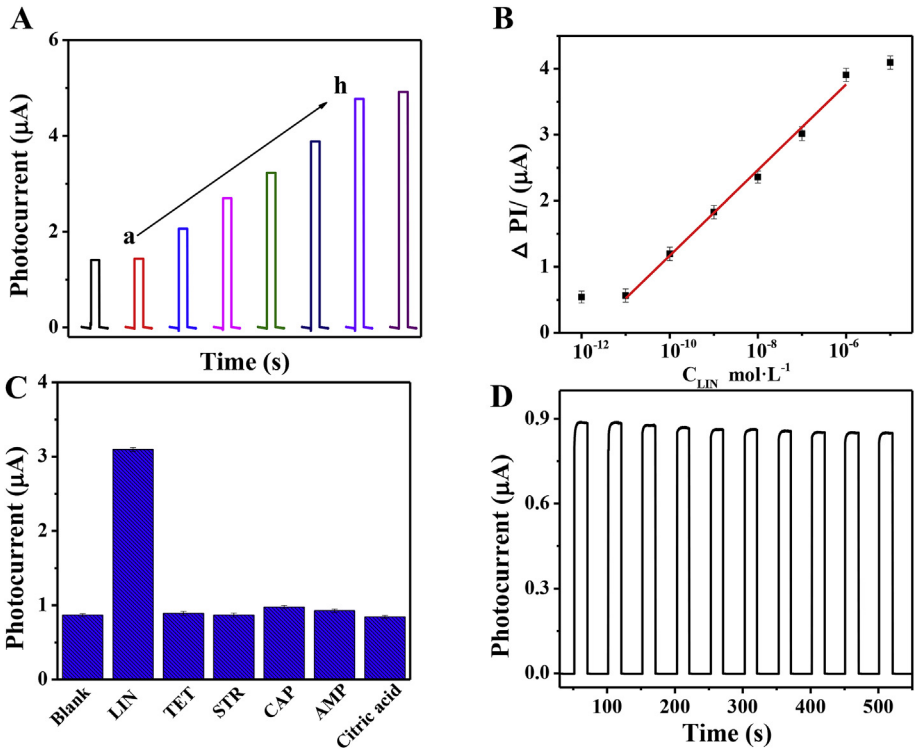

Fig. 6. (A) PEC signal of the fabricating aptasensor at different concentrations of LIN: (a→h: $10^{-12} \rightarrow 10^{-5}$ mol L^{-1}), (B) The corresponding linear calibration curve for LIN detection, (C) The selectivity of the as-fabricated aptasensor and (D) The stability measurement of the as-fabricated aptasensor under ten on/off illumination cycles.

aptasensor with substantially no significant change was recorded at ten switch irradiation cycles, and the relative standard deviation (RSD) of 3.9% was obtained, demonstrating that the fabricated PEC aptasensor is relatively stable. In addition, the PEC aptasensor was kept in reserve at 4 °C for 3 weeks, and the PEC behavior was maintained at 97.3 ± 1.2%, indicating that the as-fabricated aptasensor has good long-term stability. Meanwhile, RSD of 4.5% was acquired in a batch of freshly prepared aptamer-Bi_2MoO_6/BNG/ITO, demonstrating that the proposed aptasensor has good reproduction quality for LIN detection.

3.6. Real sample analysis

The feasibility of the proposed PEC aptasensor was verified in the milk samples by using the standard addition method. These results displayed Table S2 that the rate of recovery was in the range of 94.5 ± 2.7–115 ± 4.9% with the RSD of 2.90–4.30%, indicating proposed PEC aptasensor is feasible of for detection of real samples.

4. Conclusions

To sum up, we developed oxygen vacancies engineered Bi_2MoO_6/BNG photoactive materials as PEC functional materials via a facile one-pot solvothermal way. The introduction of BNG nanosheet can increase oxygen vacancies amounts on Bi_2MoO_6, which greatly boost the charge separation efficiency and inhibit the recombination of electron-holes, so Bi_2MoO_6/BNG nanocomposites own superior PEC performance. On the basis of specificity aptamer, the constructed PEC aptasensor displayed superior analytical property, which have a wider linear range (1×10^{-11} mol L^{-1} to 1×10^{-6} mol L^{-1}) and a lower detection limit (3.7×10^{-12} mol L^{-1}). Meanwhile, the established PEC platform was successfully employed for LIN detection in milk samples. This Bi_2MoO_6/BNG nanocomposites with oxygen vacancies as photoactive materials with visible light response, have broad application prospects in the field of food, biomedicine and analytical chemistry.

CRediT authorship contribution statement

Lan Ge: Investigation, Writing - original draft. **Qian Liu:** Methodology, Supervision. **Ding Jiang:** Writing - review & editing. **Lijun Ding:** Data curation. **Zuorui Wen:** Software. **Yingshu Guo:** Resources. **Caifeng Ding:** Formal analysis. **Kun Wang:** Supervision, Writing - review & editing.

Acknowledgements

This research was supported under the National Natural Science Foundation of China (Nos. 21375050, 21675066 and 61601204), Provincial Natural Science Foundation of Jiangsu (No. BK20160542), the Research Foundation of Zhenjiang Science and Technology Bureau (No. NY2016011) and the Foundation of Key Laboratory of Sensor Analysis of Tumor Marker, Ministry of Education, Qingdao University of Science and Technology (No. SATM201807).

Appendix A. Supplementary data

Supplementary data to this article can be found online at https://doi.org/10.1016/j.bios.2019.04.022.

References

Augugliaro, V., Garcia-Lopez, E., Loddo, V., Malato-Rodriguez, S., Maldonado, I., Marci, G., Molinari, R., Palmisano, L., 2005. Sol. Energy 79, 402–408.
Chen, W., Xu, L., Tian, Y.H., Li, H.N., Wang, K., 2018. Carbon 137, 458–466.
Chiu, M.H., Yang, H.H., Liu, C.H., Zen, J.M., 2009. J. Chromatogr. B 877, 991–994.
Choi, C.H., Park, S.H., Woo, S.I., 2012. ACS Nano 6, 7084–7091.
Du, X.J., Jiang, D., Dai, L.M., Zhu, W.R., Yang, X.T., Hao, N., Wang, K., 2018. Anal. Chem. 90, 3615–3620.
Ge, L., Li, H.N., Du, X.J., Zhu, M.Y., Chen, W., Shi, T.Y., Hao, N., Liu, Q., Wang, K., 2018. Biosens. Bioelectron. 111, 131–137.
Hao, N., Hua, R., Chen, S.B., Zhang, Y., Zhou, Z., Qian, J., Liu, Q., Wang, K., 2018. Biosens. Bioelectron. 101, 14–20.
Hao, N., Zhang, X., Zhou, Z., Hua, R., Zhang, Y., Liu, Q., Qian, J., Li, H.N., Wang, K., 2017a. Biosens. Bioelectron. 97, 377–383.
Hao, N., Zhang, Y., Zhong, H., Zhou, Z., Hua, R., Qian, J., Liu, Q., Li, H.N., Wang, K., 2017b. Anal. Chem. 89, 10133–10136.
Kecsenovity, E., Endrodi, B., Toth, P.S., Zou, Y., Dryfe, R.A.W., Rajeshwar, K., Janaky, C.,

2017. J. Am. Chem. Soc. 139, 6682–6692.
Li, L., Zhang, Y., Zhang, L.N., Ge, S.G., Liu, H.Y., Ren, N., Yan, M., Yu, J.H., 2016. Anal. Chem. 88, 5369–5377.
Li, S.H., Liu, C.H., Yin, G.H., Zhang, Q., Luo, J.H., Wu, N.C., 2017. Biosens. Bioelectron. 91, 687–691.
Liu, K., Zhu, Z.H., Li, X.J., Zhang, J.F., Yuan, X.D., Guo, C.C., Xu, W., Qin, S.Q., 2015. ACS Photonics 2, 797–804.
Liu, R., Ma, L.N., Niu, G.D., Li, X.L., Li, E.Y., Bai, Y., Yuan, G.H., 2017. Adv. Funct. Mater. 27.
Liu, Z.W., Peng, F., Wang, H.J., Yu, H., Zheng, W.X., Yang, J., 2011. Angew. Chem. Int. Ed. 50, 3257–3261.
Ma, L.B., Shen, X.P., Ji, Z.Y., Zhu, G.X., Zhou, H., 2014. Chem. Eng. J. 252, 95–103.
Meng, Q.Q., Zhou, Y.S., Chen, G., Hu, Y.D., Lv, C.D., Qiang, L.S., Xing, W.N., 2018. Chem. Eng. J. 334, 334–343.
Meng, X.C., Zhang, Z.S., 2017. Appl. Catal. B Environ. 209, 383–393.
Okoth, O.K., Yan, K., Zhang, J.D., 2017. Carbon 120, 194–202.
Qian, J., Yang, Z.T., Wang, C.Q., Wang, K., Liu, Q., Jiang, D., Yan, Y.T., 2015. J. Mater. Chem. 3, 13671–13678.
Qiu, Z., Shu, J., Tang, D., 2018. Anal. Chem. 90, 12214–12220.
Shu, J., Qiu, Z.L., Lv, S.Z., Zhang, K.Y., Tang, D.P., 2018. Anal. Chem. 90, 2425–2429.
Stypulkowska, K., Blazewicz, A., Brudzikowska, A., Grzeskiewicz, M.W., Sarna, K., Fijalek, Z., 2015. J. Pharm. Biomed. Anal. 112, 8–14.
Sun, C.Y., Xu, Q.H., Xie, Y., Ling, Y., Jiao, J.L., Zhu, H.J., Zhao, J.S., Liu, X.M., Hu, B., Zhou, D., 2017. J. Alloy. Comp. 723, 333–344.
Tian, J., Hao, P., Wei, N., Cui, H.Z., Liu, H., 2015. ACS Catal. 5, 4530–4536.
Wang, H., Yong, D.Y., Chen, S.C., Jiang, S.L., Zhang, X.D., Shao, W., Zhang, Q., Yan, W.S., Pan, B.C., Xie, Y., 2018. J. Am. Chem. Soc. 140, 1760–1766.
Wang, L.N., Liu, Z.B., Wang, D.D., Ni, S., Han, D.X., Wang, W., Niu, L., 2017. Biosens. Bioelectron. 94, 107–114.
Wang, S.B., Pan, L., Song, J.-J., Mi, W.B., Zou, J.-J., Wang, L., Zhang, X.W., 2015. J. Am. Chem. Soc. 137, 2975–2983.
Wu, J., Li, X.D., Shi, W., Ling, P.Q., Sun, Y., Jiao, X., Gao, S., Liang, L., Xu, J., Yan, W., Wang, C., Xie, Y., 2018. Angew. Chem. Int. Ed. 57, 8719–8723.
Xu, X., Ding, X., Yang, X.L., Wang, P., Li, S., Lu, Z.X., Chen, H., 2019. J. Hazard Mater. 364, 691–699.
Yan, K., Liu, Y., Yang, Y.H., Zhang, J.D., 2015. Anal. Chem. 87, 12215–12220.
Yang, C., Zhang, Z., Shi, Z., 2010. Microchim. Acta 168, 293–298.
Yang, S.B., Zhi, L.J., Tang, K., Feng, X.L., Maier, J., Müllen, K., 2012. Adv. Funct. Mater. 22, 3634–3640.
Yu, C., Fang, H.Q., Liu, Z.Q., Hu, H., Meng, X.T., Qiu, J.S., 2016. Nanomater. Energy 25, 184–192.
Yue, Z., Lisdat, F., Parak, W.J., Hickey, S.G., Tu, L., Sabir, N., Dorfs, D., Bigall, N.C., 2013. ACS Appl. Mater. Interfaces 5, 2800–2814.
Zhang, K.J., Han, P.X., Gu, L., Zhang, L.X., Liu, Z., Kong, Q.S., Zhang, C.J., Dong, S.M., Zhang, Z.Y., Yao, J.H., Xu, H.X., Cui, G.L., Chen, L.Q., 2012. ACS Appl. Mater. Interfaces 4, 658–664.
Zhang, X.J., Wang, G.S., Cao, W.Q., Wei, Y.Z., Liang, J.F., Guo, L., Cao, M.S., 2014. ACS Appl. Mater. Interfaces 6, 7471–7478.
Zhang, Y., Hao, N., Zhou, Z., Hua, R., Qian, J., Liu, Q., Li, H.N., Wang, K., 2017. Chem. Commun. 53, 5810–5813.
Zhao, W.-W., Xu, J.-J., Chen, H.-Y., 2015. Chem. Soc. Rev. 44, 729–741.
Zhao, W.W., Xu, J.J., Chen, H.Y., 2014. Chem. Rev. 14, 7421–7441.
Zheng, Y., Jiao, Y., Ge, L., Jaroniec, M., Qiao, S.Z., 2013. Angew. Chem. Int. Ed. 52, 3110–3116.
Zheng, Y., Zhou, T.F., Zhao, X.D., Pang, W.K., Gao, H., Li, S.A., Zhou, Z., Liu, H.K., Guo, Z.P., 2017. Adv. Mater. 29.
Zhou, J., Zhu, K., Xu, F., Wang, W.J., Jiang, H.Y., Wang, Z.H., Ding, S.Y., 2014. J. Agric. Food Chem. 62, 12061–12066.
Zhu, M.Y., Liu, Q., Chen, W., Yin, Y.Y., Ge, L., Li, H.N., Wang, K., 2017. ACS Appl. Mater. Interfaces 9, 38832–38841.
Zhuang, J.Y., Lai, W.Q., Xu, M.D., Zhou, Q., Tang, D.P., 2015. ACS Appl. Mater. Interfaces 7, 8330–8338.
Zou, J.-P., Ma, J., Huang, Q.H., Luo, S.-L., Yu, J., Luo, X.-B., Dai, W.-L., Sun, J., Guo, G.-C., Au, C.-T., Suib, S.L., 2014. Appl. Catal. B Environ. 156, 447–455.